

CrossMark
click for updatesCite this: *RSC Adv.*, 2016, 6, 77558

Enhanced magnetic properties and MRI performance of bi-magnetic core–shell nanoparticles

Fernando Arteaga Cardona,^{*a} Esmeralda Santillán Urquiza,^a Patricia de la Presa,^{bc} Silvia Hidalgo Tobón,^{de} Umapada Pal,^f Patricia Horta Fraijo,^g Miguel José Yacaman,^g José Daniel Lozada Ramírez,^a Robert Ivkov,^h Aracely Angulo-Molinaⁱ and Miguel Ángel Méndez-Rojas^{*a}

Two sets of bi-magnetic $Zn_{0.5}Mn_{0.5}Fe_2O_4@Fe_3O_4$ core–shell nanoparticles were prepared by a seed-mediated modified co-precipitation method. While the first set was obtained by fast addition of the alkaline solution to grow Fe_3O_4 shells over the ferrite seeds, a slow drop-wise addition of stoichiometric Fe^{2+}/Fe^{3+} ion solution to the alkaline ferrite seeds solution was adopted to synthesize the second set. Samples were characterized by electron microscopy (STEM, TEM, UHRTEM) and magnetometry measurements. Viability MTT assay of the nanoparticles on L929 murine fibroblasts were performed, indicating that they are biocompatible. The coating of the $Zn_{0.5}Mn_{0.5}Fe_2O_4$ nanoparticle by a magnetite or maghemite shell minimizes the effect of the magnetic dead layer at the core surface, improving the magnetic properties and offering thus outstanding values for biological application. Relaxometry values r_2 higher than $300 \text{ mM}^{-1} \text{ s}^{-1}$ at H 1.5 T, and cell viability at concentrations as high as 0.5 mg mL^{-1} means these bi-magnetic nanoparticles have a vast potential as MRI contrast agents.

Received 1st June 2016
Accepted 2nd August 2016

DOI: 10.1039/c6ra14265f

www.rsc.org/advances

Introduction

MRI is one of the best non-invasive analytical tools available for clinical diagnosis of several health conditions, as it can produce 2D or 3D images of soft tissues without the use of ionizing radiation, enabling widespread applications.¹ MRI contrast agents (CAs) improve sensitivity and diagnosis accuracy. CA materials enhance the detected MR signal by affecting the proton relaxation times of water molecules in their vicinity.²

Biocompatible, nanostructured magnetic CAs, with excellent stability, improved relaxometry properties, and controlled properties are attractive for their potential uses in treatment and diagnosis.^{3–5} Some nano-CAs have received approval for clinical use, such as Feridex®, Resovist®, Sinerem®, Clariscan® and Lumirem®, with a particle size of 60 to 180 nm range, good biodistribution, and biocompatibility. However, due to different reasons (symptoms such as hypotension, lumber and leg pain, vasodilatation, paresthesia reported with less than 3% of incidence; false positives and safety concerns for some of them) all of them have been withdrawn from markets except Lumirem.⁶

Due to their magnetic properties, iron oxide nanoparticles are potentially useful for therapy, diagnosis, or theranostic applications.⁷ Recently, the physics of magnetic heat generation for use in magnetic hyperthermia has been recently discussed in detail.^{8,9} Use of iron oxide nanoparticles as drug delivery agents has also been explored.¹⁰ For this purpose, frequently an engineered magnetic nanoparticle (EMN) is loaded with a drug and directed to the target tissue by applying external magnetic field or by fine-tuning the molecular recognition specificity, attaching appropriate molecules on their surfaces.

The MRI contrast (positive, T_1 -weighted, or negative, T_2 -weighted) depends on the magnetic properties of the CAs. Materials that produce darker contrast are preferred, as they will require small quantities of the CAs to produce a better image. Although most of the positive T_1 -weighted CAs are paramagnetic (e.g. gadolinium(III) chelates), superparamagnetic

^aDepartamento de Ciencias Químico-Biológicas, Universidad de las Américas Puebla, 72810 Puebla, Mexico. E-mail: fernando.arteagaca@udlap.mx; miguela.mendez@udlap.mx; Tel: +52 222 4568069; +52 222 2292607

^bInstituto de Magnetismo Aplicado, UCM-ADIF-CSIC, A6 22,500 Km, 28230 Las Rozas, Spain

^cDepartamento de Física de Materiales, UCM, Ciudad Universitaria, 28040 Madrid, Spain

^dDepartamento de Física, Universidad Autónoma Metropolitana, Avenida San Rafael Atlixco 186 Iztapalapa, Mexico City, Mexico

^eDepartamento de Imagenología, Hospital Infantil de México Federico Gómez, Dr Marquez, Col. Doctores, Mexico City, Mexico

^fInstituto de Física, Benemérita Universidad Autónoma de Puebla, Apdo. Postal J-48, Puebla, Pue. 72570, Mexico

^gDepartment of Physics and Astronomy, University of Texas at San Antonio, One UTSA Circle, San Antonio, TX 78249, USA

^hDepartment of Radiation Oncology and Molecular Radiation Sciences, Johns Hopkins University School of Medicine, Baltimore, MD 21287, USA

ⁱDepartamento de Ciencias Químico-Biológicas/DIFUS, Universidad de Sonora, Colonia Centro, 83000, Hermosillo, Sonora, Mexico

iron oxide nanoparticles are negative T_2 -weighted CAs and are an attractive option, as they possess large magnetic moments, dipolar interactions between the magnetic cores and surroundings may result in increased longitudinal and transverse relaxation rates, thus enhancing sensitivity.¹¹ Furthermore, reduced size, biocompatibility, stability and solubility in physiological conditions make them appropriate for intravenous injection. Bioconjugation of different molecules such as proteins, antibodies, peptides or sugars on their surface by simple chemistry, makes them interesting for fine-tuning their selectivity.¹² While the physical properties of magnetic nanoparticles depend on their preparation conditions, their stability depends on their size and crystallinity. Magnetic response of such particles can be controlled by substitution in the crystal lattice.

In this work, we report that simple changes in the preparation conditions of bi-magnetic core-shell nanoparticles (fast addition of an alkaline solution or slow addition of $\text{Fe}^{2+}/\text{Fe}^{3+}$ ions) affect their magnetic properties as well as their performance as MRI CAs. The bi-magnetic system, formed by growing a superparamagnetic disordered Fe_3O_4 shell on a ferromagnetic ZnMn ferrite crystalline core, will present exchange coupling among the magnetic layers, affecting their magnetic properties. Saturation magnetization and relaxometry values of the core-shell nanoparticles were higher than the values of the core alone, suggesting that engineering the architecture and composition of magnetic core-shell structures may become a simple strategy to enhance and tailor the magnetic properties and the performance of these materials for biomedical applications.^{13,14}

Methods

All the chemicals were purchased from Sigma-Aldrich (Toluca, Mexico). Manganese(II) chloride tetrahydrate ($\text{MnCl}_2 \cdot 4\text{H}_2\text{O}$, >98%), zinc chloride (ZnCl_2 , >98%), sodium hydroxide (NaOH, >97%), iron(II) chloride tetrahydrate ($\text{FeCl}_2 \cdot 4\text{H}_2\text{O}$, >98%), iron(III) chloride hexahydrate ($\text{FeCl}_3 \cdot 6\text{H}_2\text{O}$, >97%), iron(III) nitrate nonahydrate ($\text{Fe}(\text{NO}_3)_3 \cdot 9\text{H}_2\text{O}$, >98%), hydrochloric acid (HCl, 37%) and nitric acid (HNO_3 , 70%) were reagent grade and used as delivered without further purification, unless stated otherwise. Magnetic nanoparticles (MNPs) were obtained by coprecipitation, a well-known preparation method.¹⁵ Stabilization of the fabricated nanoparticles was achieved by acid peptization in aqueous media to reduce the potential aggregation/disaggregation.^{16,17}

Highly stable, water soluble, non-aggregating core-shell MNPs (10–16 nm) were obtained in aqueous solution by a two-step process. Aqueous synthesis procedures are preferable for the preparation of materials to be used in biomedical applications, as they minimize contamination with toxic reagents and bulk production can be easily achieved by scaling the preparation method. Briefly, $\text{Zn}_{0.5}\text{Mn}_{0.5}\text{Fe}_2\text{O}_4$ ferrite (ZnMn) nanoparticles were prepared following previously reported procedures.^{18–21} In a second step, ZnMn nanoparticles were used as nucleation seeds to obtain core-shell bi-magnetic nanoparticles. Two variants of this step allowed the preparation of

two different sets of products. The first one was achieved by the fast addition of alkaline NaOH solution to the 1 : 2 $\text{Fe}^{2+}/\text{Fe}^{3+}$ mixture, in the presence of the seeding ZnMn nanoparticles. The second variation consisted of the slow drop-wise addition of a 1 : 2 $\text{Fe}^{2+}/\text{Fe}^{3+}$ mixture into the alkaline dispersion of ZnMn ferrite seeds. After the completion of addition solution process, the shell forming reaction was continued for 30 minutes or two hours before it was quenched for both systems. Table 1 summarizes the preparation conditions used for each set of products. It must be emphasized that the intent of this work is to obtain and characterize core-shell nanoparticles by aqueous solution-based methods in order to ascertain their potential utility for biomedical applications.

Synthesis of Fe_3O_4 (Fe_3O_4)

Magnetite nanoparticles were prepared as follows: 2.5 mmol of $\text{FeCl}_2 \cdot 4\text{H}_2\text{O}$ was dissolved in 1 mL of distilled water with 250 μL of HCl (37%). Iron(III) chloride hexahydrate (5 mmol) was dissolved in 5 mL of distilled water, and added to the Fe^{2+} solution; then the solution containing both Fe^{2+} and Fe^{3+} was rapidly added to a NaOH 1 M solution (50 mL). The mixture was stirred for 30 minutes to form magnetite (Fe_3O_4), a black precipitate that was magnetically decanted and washed three times with distilled water.

Synthesis of $\text{Zn}_{0.5}\text{Mn}_{0.5}\text{Fe}_2\text{O}_4$ (ZnMn)

To synthesize the manganese-zinc ferrite 1.2 mmol of ZnCl_2 and 1.2 mmol of $\text{MnCl}_2 \cdot 4\text{H}_2\text{O}$ were dissolved in 1 mL of distilled water and 250 μL of HCl (37%). Iron(III) chloride hexahydrate (5 mmol) was dissolved in 5 mL of distilled water, and added to the mixture of manganese and zinc ions, then the solution containing the salts was rapidly poured into a 1 M NaOH solution (50 mL) at 100 °C. The mixture was stirred for 30 minutes, and the product was separated by magnetic decantation, washing several times with distilled water.

Synthesis of $\text{Zn}_{0.5}\text{Mn}_{0.5}\text{Fe}_2\text{O}_4@ \text{Fe}_3\text{O}_4$ by fast addition of $\text{Fe}^{2+}/\text{Fe}^{3+}$ salts (Ft, $t = 30$ m or 2 h)

Previously prepared ferrite ZnMn (0.5 g, 2.12 mmol) was dispersed in 10 mL of water and then a 2 : 1 mixture of dissolved $\text{Fe}^{2+}/\text{Fe}^{3+}$ ions was added (for $t = 30$ m, this mixture was prepared as described for the synthesis of Fe_3O_4 nanoparticles; for $t = 2$ h, the concentration of $\text{Fe}^{2+}/\text{Fe}^{3+}$ ions was doubled). After the addition had been completed, 40 mL of an aqueous 1.25 M NaOH solution was rapidly added to the reaction mixture. Finally, the black precipitate was magnetically decanted and washed several times with distilled water.

Synthesis of $\text{Zn}_{0.5}\text{Mn}_{0.5}\text{Fe}_2\text{O}_4@ \text{Fe}_3\text{O}_4$ by slow addition of $\text{Fe}^{2+}/\text{Fe}^{3+}$ salts (Dt, $t = 30$ m or 2 h)

Previously prepared ferrite ZnMn (0.5 g, 2.12 mmol) was dispersed in 50 mL of a 1 M NaOH solution. Then, a 2 : 1 mixture of $\text{Fe}^{2+}/\text{Fe}^{3+}$ ions was slowly added drop-wise at a rate of 100 $\mu\text{L min}^{-1}$. The concentration of the mixture of iron ions was as previously described for $t = 30$ m or $t = 2$ h. Finally, the black

Table 1 Summary of the synthesis procedure. Core reaction time is 30 min for all the samples

Sample name	Chemical composition	Shell reaction time	Mode of addition of Fe ions for shell formation
Fe ₃ O ₄	Fe ₃ O ₄	—	—
ZnMn	Zn _{0.5} Mn _{0.5} Fe ₂ O ₄	—	—
F30m	Zn _{0.5} Mn _{0.5} Fe ₂ O ₄ -Fe ₃ O ₄	30 minutes	Fast
F2h	Zn _{0.5} Mn _{0.5} Fe ₂ O ₄ -Fe ₃ O ₄	2 hours	Fast
D30m	Zn _{0.5} Mn _{0.5} Fe ₂ O ₄ -Fe ₃ O ₄	30 minutes	Drop-wise
D2h	Zn _{0.5} Mn _{0.5} Fe ₂ O ₄ -Fe ₃ O ₄	2 hours	Drop-wise

powder was separated by magnetic decantation and washed several times with distilled water.

Aqueous stabilization by acid peptization

Briefly, 25 mL of 2 M HNO₃ was added to the washed MNPs and stirred for 15 minutes. Then, the aqueous acidic supernatant was magnetically decanted, and 5 mL of iron(III) nitrate nonahydrate (1 M) solution and 20 mL of water were added and boiled for 25 minutes. After that time, the supernatant was magnetically decanted. Finally, 25 mL of 2 M HNO₃ was added to the sample and left stirring for 15 minutes, then the product was separated by magnetic decantation and washed with acetone. Finally, samples were re-dispersed in water.

Characterization

Particle and aggregate size

Particle size and shape of the synthesized nanostructures were analyzed using a JEOL JEM1010, a JEOL 1230 and an aberration-corrected JEOL ARM 200F ultra-high resolution transmission electron microscope, UHRTEM (JEOL USA, Inc., Peabody, MA) located at the ICMM-CSIC and the Kleberg Advanced Microscopy Center-UTSA, respectively. Scanning transmission electron microscope (STEM) images were acquired using a Hitachi STEM S5500 (Hitachi High-Technologies Co., Tokyo, JP) equipped with an energy-dispersive spectroscopy (EDS) detector. The average particle size was measured by counting more than 200 particles of each sample individually and fitted with a lognormal distribution to calculate the mean size and the standard deviation. Size dispersion and the hydrodynamic diameter of the samples were measured at room temperature using dynamic light scattering (DLS) instrument NanoFlex (Microtrac Inc., Montgomeryville, PA, USA), with a 780 nm wavelength red laser of 3 mW.

XRD analysis

X-ray diffraction (XRD) patterns were measured by Powder Diffractometer Bruker D8 Advance with Cu K α radiation with energy-discriminator (solx). The X-ray patterns were collected between 15° and 80° of 2 θ .

Chemical composition

Determination of ratio of Mn(II), Zn(II) and total Fe ions was carried out using an inducing coupling plasma optical emission spectrometer (ICP-OES), OPTIME 2100DV from Perkin Elmer. The wavelengths used to determine the transition metal ions were 257.61, 206.2 and 238.20 nm. Since some elements can interfere with the iron measurements, another wavelength was used (239.56 nm) to have a higher precision for the evaluation of iron contain. For this purpose, 50 μ L of the samples were digested by using a solution of HNO₃ : HCl (3 : 1). The concentration was adjusted to be 10 ppm, and the values of intensity were compared to a previously made calibration curve to obtain the mass of each ion. The results were adjusted to the Mn mass, considering the stoichiometry for the ZnMn ferrite (Zn_{0.5}Mn_{0.5}Fe₂O₄). Table 2 shows the adjusted number of moles according to the ICP-OES analysis for samples F30m and F2h; it can be noted that the iron concentration increases when the Fe₃O₄ shell formation reaction passes from 30 min to 2 h. This increase can be attributed to a thicker magnetite shell growing over the ZnMn nanoparticle core.

Magnetic characterization

Hysteresis curves (room temperature and 10 K) of the samples were recorded in a magnetic field up to 5 T for hysteresis curves. Zero field cooled–field cooled (ZFC–FC) measurements were done with a magnetic field of 200 Oe. A vibrating sample magnetometer (VSM) attached to a Physical Property Measurements System (PPMS, Quantum Design, Dyna-cool 9, USA) was used for all the magnetic measurements by placing the sample into tubular plastic sample holders. The approximate magnetic diameters of the samples at 300 K were calculated using Chantrell's equation (eqn (1)):²²

$$D_{\text{mag}} = \left[\frac{18k_{\text{B}}T}{\pi M_{\text{s}}} \left(\frac{\chi_{\text{ini}}}{3m_{\text{s}}} \frac{1}{H_0} \right)^{\frac{1}{2}} \right]^{\frac{1}{3}} \quad (1)$$

where k_{B} represents the Boltzmann constant, T is the temperature in K, M_{s} is the bulk saturation magnetization of the sample (for the core–shell systems the saturation of the manganese ferrite was used), χ_{ini} is the initial susceptibility at low fields, m_{s} is the saturation magnetization of the sample and $1/H_0$ is the M at 0 field, estimated by extrapolation.

Performance as MRI contrast agents

Relaxometry of the samples was determined in a clinical 1.5 T MRI scanner (Philips Intera-Achieva (Philips Healthcare, Best, Netherlands)). Samples were dispersed in a 6.6 mg mL⁻¹ agar solution; the concentration of the samples was adjusted to

Table 2 Stoichiometry analysis of the ion mass, according to the ICP-OES results

Sample	Mn	Zn	Fe (core)	Fe (shell)
F30m	0.50	0.37	2.00	3.90
F2h	0.50	0.52	2.00	8.98

0.025, 0.050, 0.075, 1.000 and 1.025 mg in 15 mL plastic tubes. The r_2 values were calculated using a multi-fast field echo sequence (mFFE) from 4.6 to 104.6 ms TE; intensity contrast of the images was obtained using OsiriX software (Pixmeo, Geneva, Switzerland).²³ For r_2 calculation, first the data were adjusted to an exponential decay equation (eqn (2)), and then the rate values ($R_2 = 1/T_2$) were plotted against the total ion concentration of the samples in mM to obtain the relaxometry (r_2) values from the slope of the graph:

$$S_{TE} = S_0 e^{-\frac{TE}{T_2}} \quad (2)$$

where S_{TE} is the intensity at a determined time echo, S_0 is the initial intensity.

Cell culture

Cell line L929 (mouse fibroblast derived from adipose tissue) obtained from the American Type Culture Collection (ATCC, Rockville, MD) was used in this study. The cells were maintained in Dulbecco's modified Eagle's medium (DMEM) supplemented with 5% fetal bovine serum (FBS), 1% penicillin-streptomycin, and 1% glutamine at 37 °C and 5% CO₂ atmosphere during 24 h. Cells were seeded in triplicate at a density of 10 000 on 96-well culture plates and incubated for 24 h before the experiments.²⁴

In vitro viability assay

The L929 cells were exposed to different concentrations of nanoparticles previously suspended in culture media and serially diluted (0–1000 μg mL⁻¹). For measuring cell viability after exposition to the prepared nanoparticles, a MTT (3-[4,5-dimethylthiazol-2-yl]-2,5 diphenyl tetrazolium bromide) colorimetric assay was utilized at 24 and 48 h. After the incubation period, sample solutions were removed, rinsed with PBS and MTT solution (5 mg mL⁻¹ in PBS pH 7.4) was added to all the wells and incubated for 4 h at 37 °C in the dark. Then, 100 μL of 0.004 N HCl in isopropanol was added to each well to the lysate. Absorbance was monitored in a microplate reader at a wavelength of 550 nm. Untreated cells were considered as controls.²⁴ The cell viability was calculated as:

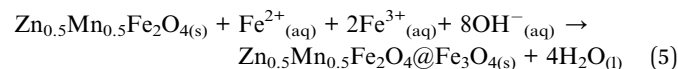
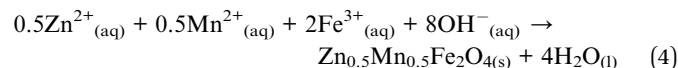
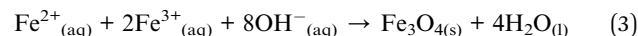
$$\% \text{ cell viability} = \left(\frac{\text{absorbance of sample well}}{\text{absorbance of control well}} \right) \times 100$$

Analysis of results was done with the program GraphPad Prism 5 for the calculation of viability curves. Results were expressed as mean values ± SEM (standard error of the mean) in triplicate.

Results and discussion

The methods used to prepare core-shell MNPs in this work are based on colloidal wet chemistry, which has been widely studied.^{25,26} Eqn (3)–(5), describe the chemical reactions that yield the magnetic materials fabricated in this study. Water soluble, highly stable, non-aggregating MNPs could be obtained

with an excellent control of size and size dispersity, as shown in Table 2.



Structural characterization

Fig. 1 presents the TEM images and size distribution histograms of the samples. As expected, core-shell MNPs have larger sizes than the first ZnMn nanoparticles used as seeds, as well as different polydispersity. Table 3 summarizes the results of average nanoparticle sizes as determined by several methods (TEM, DLS, and magnetic measurements), as well as polydispersity index (PI). The sample F30m shows the highest polydispersity in comparison to the other samples. This increase in the polydispersity may indicate that the process of shell formation competes with the nucleation process, producing a more random and polydisperse shell structure.²⁰ After 2 hours of shell formation, the polydispersity decreases to 0.19 and the nanoparticle size increases to 12.3 nm. In contrast, slow, drop-wise addition of the Fe²⁺/Fe³⁺ mixture leads to a lower polydispersity and a larger particle size (see Table 3). The fast addition of the Fe²⁺/Fe³⁺ mixture may create

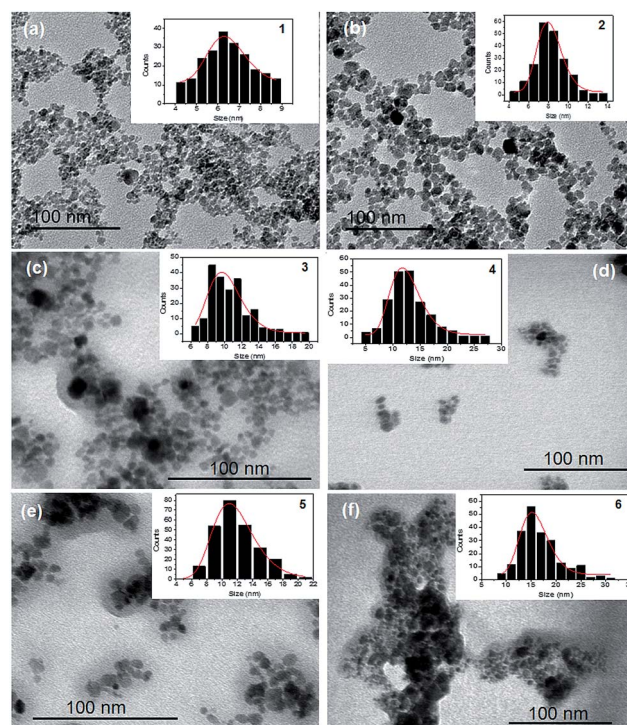


Fig. 1 TEM and STEM images of samples (a) Fe₃O₄, (b) ZnMn, (c) F30m, (d) F2h, (e) D30m and (f) D2h with their size distribution fitted using a lognormal function.

Table 3 Average size values as determined by TEM (D_{TEM}), DLS (D_{H}) and magnetic characterization (D_{mag}), and their polydispersity index (PI)^a

Sample	D_{TEM} (nm)	D_{H} (nm)	PI (D_{H})	D_{mag} (nm)
Fe ₃ O ₄	6.4 ± 0.2	23.2 ± 7.9	0.34	5.6
ZnMn	8.0 ± 0.2	20.3 ± 7.7	0.38	6.3
F30m	10.0 ± 0.3	27.0 ± 11.1	0.41	8.8
F2h	12.3 ± 0.2	28.6 ± 9.1	0.32	7.8
D30m	11.5 ± 0.2	29.0 ± 9.8	0.34	10.5
D2h	15.6 ± 0.1	25.0 ± 6.5	0.26	8.7

^a PI = SD/mean.

a disordered and non-uniform shell, composed of smaller particles compared to a more controlled and uniform layers due to the slow drop-by-drop addition of precursors. This observation is consistent with previously published findings, where the effect of the fast or slow addition of the alkaline solution on the formation of magnetite was studied.²⁷ In that work, smaller magnetite nanoparticles were obtained by fast addition of a NaOH solution, in contrast to those obtained by slow addition of the base. The degree of polydispersity and crystallinity of growing crystallites were affected by physical variables such as temperature, concentration of reagents, quenching reaction time and reagent addition rate.²⁸ The rate of addition of the base solution affects the ordering (crystallinity) of the magnetic shell layer forming on the surface of the ZnMn nanoparticles used as seeds, which in turns affects the magnetic properties.²⁹ All samples present low polydispersity (Table 3), the highest polydispersity index (PI) value being 0.24 for sample F30m, well below 0.3, the limiting PI value recommended for biomedical applications.²⁹

Fig. 2a, UHRTEM image of sample D2h, clearly shows a close packed cubic structure. Fe₃O₄ is a ferromagnetic material which crystallizes within a spinel cubic structure, so these images are in agreement with the expected for a magnetite shell. The

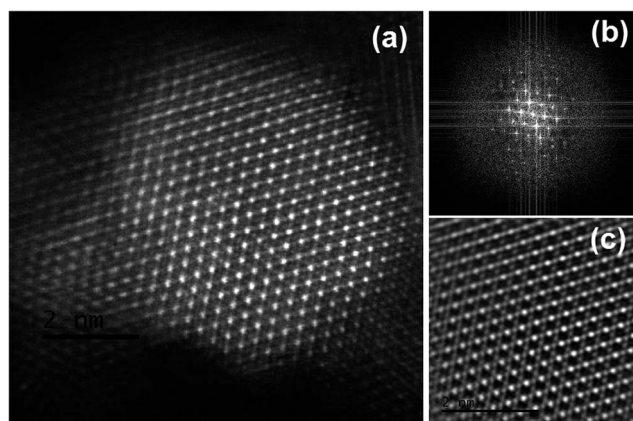


Fig. 2 UHRTEM image of sample D2h. (a) Bright field image showing the characteristic cubic close-packed structure; (b) FFT pattern indicating a typical pattern for cubic crystals; (c) filtered image, showing clearly the cubic array; the $\langle 110 \rangle$ zone axis can be appreciated, which is in agreement with the FFT pattern.

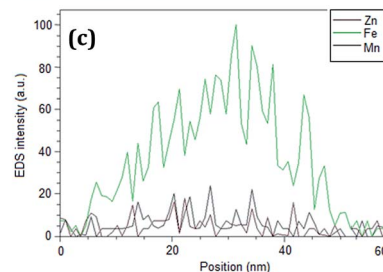
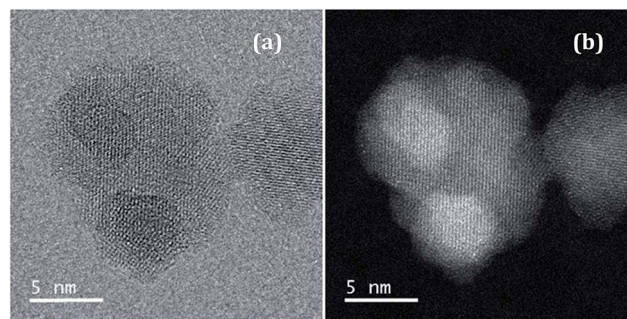


Fig. 3 UHRTEM (a) bright and (b) dark field images of a selected particle of sample D2h, showing a core-shell structure; (c) EDS linear profile of a particle, confirming a Zn–Mn rich core and a Fe rich shell.

corresponding FFT pattern in Fig. 2b arise from the adjacent region in the shell; the image clearly shows the structure of the shell, but the core can't be solved due to probable different crystal orientation.⁴⁷ XRD analyses (Fig. 5) confirmed that the nanoparticles are in the nanocrystalline cubic spinel phase. The noisy XRD diffractograms for samples F30m and D30m suggest that the Fe₃O₄ shell formed on the surface of the ZnMn ferrite core is disordered or amorphous. These results are similar to those reported by Song and coworkers for a series of magnetically active ferrite NPs prepared by growing a Fe₃O₄ shell on Mn oxide NPs used as seeds.²⁷

Fig. 3 presents TEM images for a selected nanoparticle from sample D2h, in bright (Fig. 3a) and dark (Fig. 3b) fields. EDS analysis along a horizontal line crossing through the particle (Fig. 3c) suggests a composition that resembles the expected core-shell structure, based on the changes in Fe, Zn, and Mn concentration along the length of measurement. We note that

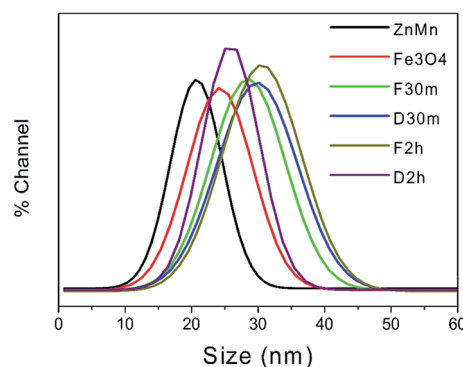


Fig. 4 Particle size distribution of aqueous suspensions of magnetic and bi-magnetic core-shell nanoparticles determined by DLS.

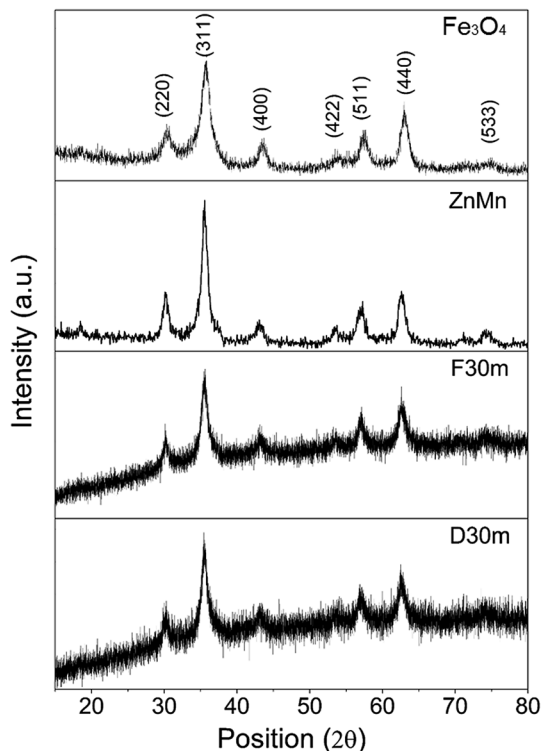


Fig. 5 XRD patterns of the core and shell alone (top), and the bi-magnetic core-shell structures D30m and F30m (bottom).

Table 4 Magnetic properties of the samples, the % increase values were calculated using the core (ZnMn) as a reference

Samples	M_{sat} (emu g ⁻¹)		M_{sat} % increase		T_{B} (K)	H_{c} (Oe) at 10 K
	300 K	10 K	300 K	10 K		
Fe ₃ O ₄	37.72	47.21	—	—	112	271
ZnMn	42.37	77.22	—	—	123	150
F30m	49.21	71.38	16.14%	-7.56%	219	164
F2h	53.13	71.04	25.39%	-8.00%	168	184
D30m	43.65	68.05	3.02%	-11.87%	176	260
D2h	50.69	66.29	19.63%	-14.15%	217	250

UHRTEM images do not enable us to distinguish clearly the core from the shell in the Fe₃O₄/ZnMn system, as the magnetite shell grows over the ZnMn ferrite core, and both have similar crystal structures. On the other hand, EDS data (Fig. 3c) and information obtained from ICP (Table 2) and XRD (Fig. 5) suggest that a disordered core-shell structure was achieved by this modified co-precipitation method. The synthetic methodology to get these nanostructured systems through the modified co-precipitation of a magnetite shell on the ZnMn seed/core under different conditions especially the rate of precursor addition seems to play a major role in achieving these highly disordered core-shell structures. The shell may be composed by nanocrystallites growing on the core surface, as Fig. 3a and b seem to indicate.

As can be seen from Fig. 4, the hydrodynamic size particles are smaller than 35 nm, suggesting well-dispersed nanoparticles as expected for non-aggregated samples stabilized by acid peptization. It has been reported that the MRI performance may be affected by the use of polymeric coatings as surfactants,³⁰ due to a variety of inter-particle weak interactions that may induce aggregation and dipolar interactions between particles.³¹

XRD diffraction patterns do not show any significant difference between samples ZnMn and Fe₃O₄ with respect to the core-shell samples, as both the core and the shell have the same crystal structure. Although both crystal structures are the same (mixed spinel) and have different interplanar distances because of their different composition, the resulting diffraction peaks become broader compared to the pure Fe₃O₄ or ZnMn samples (Fig. 5). This effect is probably due to the loss of long range ordering at the particle surface.

Magnetic characterization

As expected for a core-shell structure, the calculated magnetic size of the samples, shown in Table 4, are smaller than the particle size determined by TEM. This decrease in size is a consequence of interfacial defects such as a magnetic dead layer (MDL) (originated by vacancies, dangling bonds, and

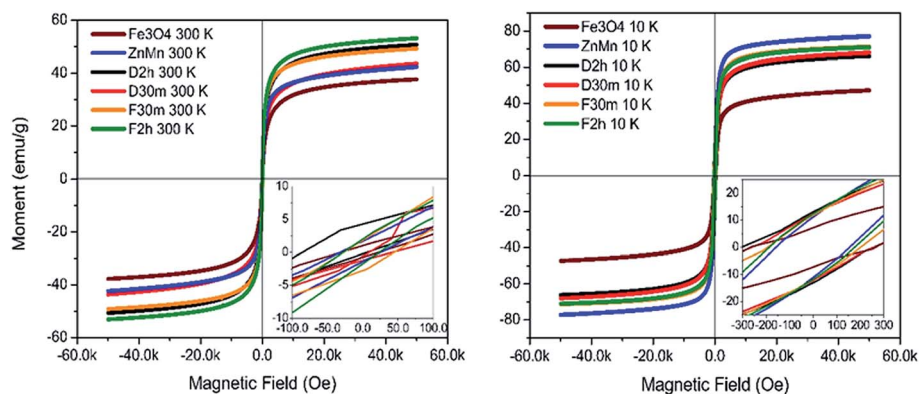


Fig. 6 Hysteresis loops for all samples at $T = 300$ K (left) and 10 K (right) showing clearly an enhanced magnetization saturation compared to sample ZnMn (core), also a decrease in M_{s} at 10 K with respect to the core. Insets show negligible coercivity at 300 K (superparamagnetic state) and wider loops at 10 K (blocked state).

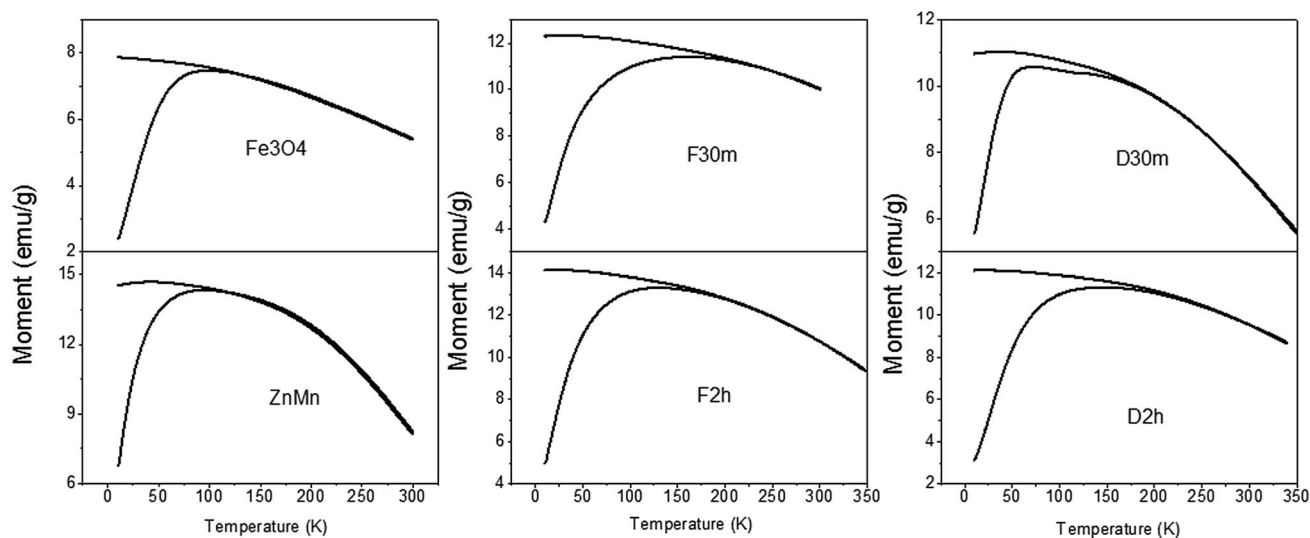


Fig. 7 ZFC-FC graphs of the samples at 200 Oe.

disorder on the layer) which diminishes the effective volume of the MNPs contributing to the magnetism.^{27,32} Moreover, that calculated magnetic size is just a theoretical approximation to the real size of the magnetic contribution of the nanoparticles.^{33,34}

One of the most surprising results of this work is the increase by 25% of saturation magnetization of the core-shell structure in F2h regarding the corresponding individual values of the

ZnMn (core) or Fe_3O_4 (shell) (Table 4). This improvement is observed especially at room temperature, which is the temperature range of interest for any biological application.

On the other hand, the systems obtained by slow, dropwise addition of the $\text{Fe}^{2+}/\text{Fe}^{3+}$ mixture have small increments of M_s , just about 3% and 19% after 30 minutes and 2 hours of synthesis, respectively. In comparison, core-shell MNPs obtained by the fast addition of alkaline solution method

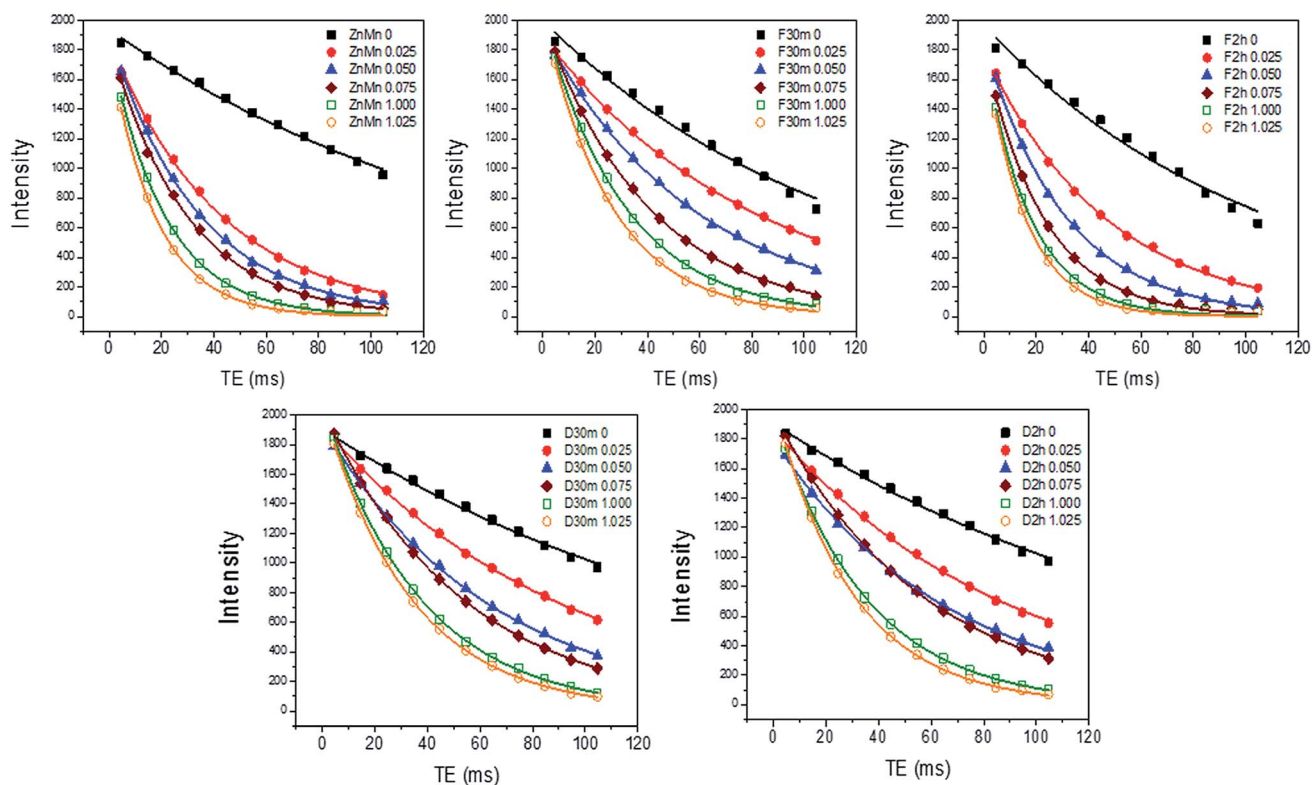


Fig. 8 Signal intensity exponential decay curves measured at different TE from 4.6 to 104.6 ms.

presented increments of 18% and 25%, after 30 minutes and 2 hours, respectively.

For the core-shell systems, the M_s at 10 K are lower than the corresponding value for the ZnMn ferrite core. The saturation magnetization decreases up to 14% in the core-shell systems with respect to ZnMn; however, their M_s at 300 K are nearly 25% higher. The existence of a shell with antiparallel spins (with respect to the core spins) dispersed in the system might be responsible for this behavior at low temperature. Although thermal fluctuations may be sufficient to allow these antiparallel spins to shift and reverse partially to each other at 300 K, at 10 K the heat energy is insufficient to induce these thermal fluctuations, and the shell spins align antiparallel to the core spins diminishing the values of M_s in the core-shell systems. The later may explain the differences observed in the hysteresis curves at 300 K and 5 K (insets, Fig. 6). It has been previously reported that competing interactions among magnetic layers or uncompensated spins at the interface in core-shell systems may induce the spins to be antiferromagnetically aligned, resulting on net magnetization and affecting the M_s values.^{35,36}

Exchange coupling interactions between magnetic layers may explain the enhancement in M_s at 300 K. Increments and variations of the magnetic properties of bi-magnetic structures has been reported previously for ferromagnetic/antiferromagnetic (FM/AFM) and antiferromagnetic/ferromagnetic (AFM/FM) core-shell systems.^{37–40}

The differences in magnetic behavior among the core-shell samples obtained by both methods may be explained by the exchange coupling between the magnetic core and the magnetic shell. The spin coupling arises from the effect of dipolar interactions between the magnetic core and the shell.⁴¹ It is well known that the dipolar effect has a significant influence on the magnetic properties of materials. For bi-magnetic core-shell systems, the whole core is in full contact with the shell, while the surrounding MNPs may also contribute to these magnetic interactions. Eqn (6) clearly state that the energy of the dipole

Table 5 r_2 values of the samples, and their % increase with respect to the core (ZnMn)

Sample	r_2 (mM ⁻¹ s ⁻¹)	% increase
ZnMn	262.62	—
F30m	323.05	23.01
F2h	386.61	47.21
D30m	194.91	-25.78
D2h	242.55	-7.64

changes by increasing the magnetic moment and decreasing the interparticle distance.⁴²

$$E_d \approx \frac{\mu_0 \mu^2}{4\pi d^3} \quad (6)$$

where E_d is the energy of the dipole, μ_0 is the permeability of free space, μ is the average magnetic moment and d is the distance between dipoles.

The changes observed in magnetic properties for the two different sets of magnetic core-shell nanoparticles suggest that the slow addition of the iron salts may produce a thick MDL, which decreases the exchange coupling between the core and the shell. On the other hand, the fast addition of alkaline solution seems to favor the rapid nucleation of magnetite on the seed surface, creating a thin MDL, decreasing the distance between the magnetic layers, and increasing the MNP polydispersity. After 30 min or 2 h of reaction, homogenization of the shell thickness occurs in both cases, with no significant change in their magnetic properties (Table 4). As the shell becomes thinner, the effective core-shell interface becomes larger and the exchange coupling increases.⁴³

Blocking temperature (T_B) was approximated from the ZFC-FC curves (Fig. 7), and values are shown in Table 4. The T_B values remain significantly low suggesting that the MNPs may flip their spins, reversing their net magnetization at room temperature and above. The reversal of magnetization might be of fundamental importance as heat generation in magnetic hyperthermia occurs by Néel relaxation.

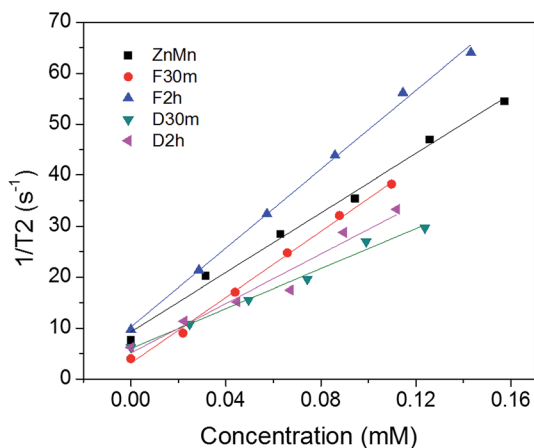


Fig. 9 Linear relationship of R_2 values plotted against the concentration of total ions used to calculate the relaxometry (r_2) values for all the samples.

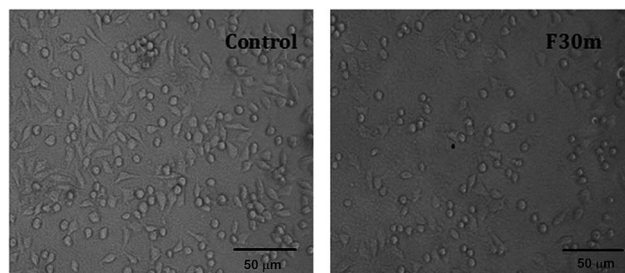


Fig. 10 L929 cells morphology. The cells were exposed at 0–1000 $\mu\text{g mL}^{-1}$ of nanoparticles F30m for 24 and 48 h. The pictures were taken at the highest dose (1000 $\mu\text{g mL}^{-1}$) after 48 h. L929 cells treated with F30m during 48 h showed the altered morphology of damaged cells just in 1000 $\mu\text{g mL}^{-1}$. The control was untreated cells. All treatments were dispersed in culture media. Inverted microscope with 20 \times magnification.

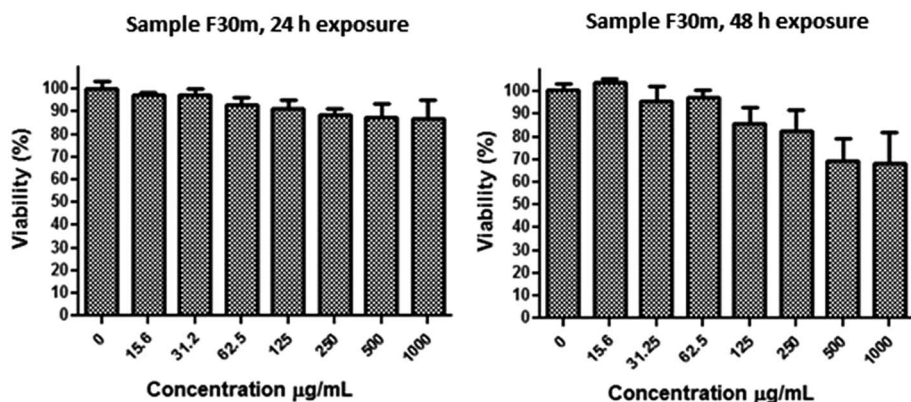


Fig. 11 Cell viability evaluated by MTT assays. Left: sample F30m at 24 h of exposure. Right: sample F30m at 48 h of exposure. The viability was affected only by the highest doses of F30m.

Performance as MRI T_2 contrast

A 1.5 T MRI instrument was used to measure the signal decay. The samples total mass concentrations were adjusted to be from 0.025 mg to 1.025 mg. Fig. 8 shows the exponential decay of the signal of water, the higher the concentration, the faster the signal decay is. Zero concentration in some cases adopts what it may seem a linear decay. Rate ($R_2 = 1/T_2$) values were acquired by fitting decay of the intensity signal to a monoexponential decay ($S_{TE} = S_0 e^{-TE/T_2}$),⁴⁴ and rate values were plotted against the concentration values giving a linear response.⁴⁵ The slopes of the fitted linear plots (Fig. 9) are the relaxation values (r_2). Relaxation values of the samples are summarized in Table 5.

Although an agglomeration of nanoparticles is known to increase the r_2 signal intensity,⁴⁶ our systems can be considered monodispersed (as seen from the DLS analysis) and have no significant agglomeration (Fig. 4).

Sample F2h has the highest r_2 value among all samples. It is interesting to note that the sample with the highest M_s value also has the highest r_2 indicating that the field inhomogeneities introduced by the MNPs have a higher dependency to the M_s values of the magnetic materials. The increase in the r_2 value of sample F2h was almost 50% respect to the core ZnMn sample. On the other hand, the samples synthesized by slow addition decreased the r_2 values 25% in both cases (at 30 minutes and 2 hours), even though the slow addition D30 samples had higher M_s values than ZnMn. This reduction in the r_2 values was completely unexpected and other parameters, aside of M_s and aggregation, also played a crucial part in making the precession movement of the water protons slower. The later suggest that the T_2 contrast performance of all core-shell samples may be optimized by controlling aggregation and fine-tuning of their M_s values primarily.

Cell culture and *in vitro* viability assay

Morphology. Effects of exposition of test cells to F30m, a sample considered to be representative of all the samples fabricated in this study, were followed using inverted microscopy at 24 and 48 h after treatment. Cells exposed to F30m maintained their normal morphology in all the cases, including

for the highest evaluated concentration, after 24 h of exposure. However, treatment with F30m induced some morphological changes at the highest doses on 48 h of exposure (500–1000 $\mu\text{g mL}^{-1}$) (Fig. 10). In previous work, we demonstrated that a nanoparticle concentration less than 500 $\mu\text{g mL}^{-1}$ had no effect on the cell morphology.²⁴ The results obtained from the evaluation of cell viability indicate that the sample F30m is biocompatible.

Viability. Results of this study indicate almost 90% of viability at 24 h of exposure to F30m, even at high concentrations, suggesting biocompatibility during this period of incubation. However, at 48 h of exposure to F30m, the viability was affected only at the highest doses (500–1000 $\mu\text{g mL}^{-1}$), where the cells showed nearly 70% of viability (Fig. 11). These results suggest that the evaluated nanoparticles present biocompatibility in most of the usual concentration ranges used for biomedical purposes (<500 $\mu\text{g mL}^{-1}$).

Conclusion

In summary, we demonstrate that different preparation pathways (fast addition of NaOH or slow, drop-wise addition of iron precursors) can induce significant differences in the magnetic properties of core-shell bi-magnetic nanoparticles, affecting considerably their M_s values and relaxivity, which determine their MRI performance as contrast agents. Fast addition of alkaline solution produces bi-magnetic core-shell nanoparticles of superior magnetic properties with respect to those of magnetite cores. While the core-shell nanostructures prepared by fast addition of alkaline solution and 30 min reaction time (sample D30m) have 25% higher M_s values than the core alone, the sample prepared at 2 h reaction time (sample D2h) has better r_2 value, indicating an improved MRI performance than the other systems. Also, all the nanoparticles presented good responses under using a 1.5 T MRI scan, which is the most common MRI equipment that hospitals have. For the samples synthesized by slow addition of iron ions, the variations in magnetic properties were modest. These differences can be attributed to a magnetic exchange interaction between the core and the shell, suggesting that changes in the structure of the interface between the core and the shell may play

a significant role in the exchange interactions. The MDL could get thicker or thinner, depending on the synthetic conditions, affecting the exchange interaction between the magnetic layers. To maximize this interaction between the magnetic layers, the preparation methodology for bi-magnetic core-shell nanostructures must produce a disordered interface as thin as possible, favoring a more efficient exchange coupling between the spins of the core and the shell. Performed *in vitro* cell viability assays indicate that the core-shell nanoparticles are biocompatible, with no adverse effect on cells for concentrations up to $500 \mu\text{g mL}^{-1}$. The usefulness of the fabricated bi-magnetic nanostructures as MRI contrast agent under available clinical conditions (using a 1.5 T scanner) has been demonstrated. Further work on the development of bi-magnetic core-shell systems useful as MRI contrast agent, and for hyperthermal therapy is in progress.

Acknowledgements

The work was supported by CONACYT (Grants # CB-2010/154602, CB-2010/151767, and INFR-2014-02-230530) and the Spanish Ministry of Science and Innovation (MAT2012-37109-C02-01). SHT thanks, Hospital Infantil de México Federico Gómez for access to its clinical MRI facilities.

References

- H. Shokrollahi, A. Khorramdin and G. Isapour, Magnetic Resonance Imaging by Using Nano-Magnetic Particles, *J. Magn. Magn. Mater.*, 2014, **369**, 176–183.
- M. Wabler, W. Zhu, M. Hedayati, A. Attaluri, H. Zhou, J. Mihalic, A. Geyh, T. L. DeWeese, R. Ivkov and D. Artemov, Magnetic Resonance Imaging Contrast of Iron Oxide Nanoparticles Developed for Hyperthermia Is Dominated by Iron Content, *Int. J. Hyperthermia*, 2014, **30**, 192–200.
- D. K. Kim, Y. Z. J. Kehr, T. Klason, B. Bjelke and M. Muhammed, Characterization and MRI Study of Surfactant-Coated Superparamagnetic Nanoparticles Administered into the Rat Brain, *J. Magn. Magn. Mater.*, 2001, **225**, 256–261.
- H. Hejase, S. S. Hayek, S. Qadri and Y. Haik, MnZnFe Nanoparticles for Self-Controlled Magnetic Hyperthermia, *J. Magn. Magn. Mater.*, 2012, **324**, 3620–3628.
- M. Levy, C. Wilhelm, J. M. Siaugue, O. Horner, J. C. Bacri and F. Gazeau, Magnetically Induced Hyperthermia: Size-Dependent Heating Power of Gamma-Fe₂O₃ Nanoparticles, *J. Phys.: Condens. Matter*, 2008, **20**, 204133.
- Y.-X. J. Wang, Superparamagnetic Iron Oxide Based MRI Contrast Agents: Current Status of Clinical Application, *Quant. Imag. Med. Surg.*, 2011, **1**, 35–40.
- D. Yoo, J.-H. Lee, T.-H. Shin and J. Cheon, Theranostic Magnetic Nanoparticles, *Acc. Chem. Res.*, 2011, **44**, 863–874.
- D. Ortega and Q. A. Pankhurst, Magnetic Hyperthermia, in *Nanoscience: Volume 1: Nanostructures through Chemistry*, The Royal Society of Chemistry, 2013, vol. 1, pp. 60–88.
- C. L. Dennis and R. Ivkov, Physics of Heat Generation Using Magnetic Nanoparticles for Hyperthermia, *Int. J. Hyperthermia*, 2013, **29**, 715–729.
- X. Mou, Z. Ali, S. Li and N. He, Applications of Magnetic Nanoparticles in Targeted Drug Delivery System, *J. Nanosci. Nanotechnol.*, 2015, **15**, 54–62.
- M. P. Morales, O. Bomati-Miguel, R. Pérez de Alejo, J. Ruiz-Cabello, S. Veintemillas-Verdaguer and K. O'Grady, Contrast Agents for MRI Based on Iron Oxide Nanoparticles Prepared by Laser Pyrolysis, *J. Magn. Magn. Mater.*, 2003, **266**, 102–109.
- E. Santillán-Urquiza, F. Arteaga-Cardona, E. Hernández-Herman, P. F. Pacheco-García, R. González-Rodríguez, J. L. Coffey, M. E. Mendoza-Alvarez, J. F. Vélez-Ruiz and M. A. Méndez-Rojas, Inulin as a Novel Biocompatible Coating: Evaluation of Surface Affinities toward CaHPO₄, α -Fe₂O₃, ZnO, CaHPO₄@ZnO and α -Fe₂O₃@ZnO Nanoparticles, *J. Colloid Interface Sci.*, 2015, **460**, 339–348.
- P. Crespo, P. de la Presa, P. Marin, M. Multigner, J. M. Alonso, G. Rivero, F. Yndurain, J. M. Gonzalez-Calbet and A. Hernando, Magnetism in Nanoparticles: Tuning Properties with Coatings, *J. Phys.: Condens. Matter*, 2013, **25**, 484006.
- V. Dupuis, V. Gavrilov-Isaac, S. Neveu, M. Aouadi and S. Abramson, Synthesis and Properties of Magnetic Nanoparticles with Tunable Magnetic Anisotropy Energy, *Mater. Res. Soc. Symp. Proc.*, 2014, **1708**, 1708.
- M. Mascolo, Y. Pei and T. Ring, Room Temperature Coprecipitation Synthesis of Magnetite Nanoparticles in a Large Ph Window with Different Bases, *Materials*, 2013, **6**, 5549–5567.
- E. Auzans, D. Zins, E. Blums and R. Massart, Synthesis and Properties of Mn–Zn Ferrite Ferrofluids, *J. Mater. Sci.*, 1999, **34**, 1253–1260.
- F. Arteaga-Cardona, K. Rojas-Rojas, R. Costo, M. A. Mendez-Rojas, A. Hernando and P. de la Presa, Improving the Magnetic Heating by Disaggregating Nanoparticles, *J. Alloys Compd.*, 2016, **663**, 636–644.
- T. Ahn, J. H. Kim, H.-M. Yang, J. W. Lee and J.-D. Kim, Formation Pathways of Magnetite Nanoparticles by Coprecipitation Method, *J. Phys. Chem. C*, 2012, **116**, 6069–6076.
- C. Ravikumar and R. Bandyopadhyaya, Mechanistic Study on Magnetite Nanoparticle Formation by Thermal Decomposition and Coprecipitation Routes, *J. Phys. Chem. C*, 2011, **115**, 1380–1387.
- N. T. K. Thanh, N. Maclean and S. Mahiddine, Mechanisms of Nucleation and Growth of Nanoparticles in Solution, *Chem. Rev.*, 2014, **114**, 7610–7630.
- R. Massart, Preparation of Aqueous Magnetic Liquids in Alkaline and Acidic Media, *IEEE Trans. Magn.*, 1981, **17**, 1247–1248.
- R. Chantrell, J. Popplewell and S. Charles, Measurements of Particle Size Distribution Parameters in Ferrofluids, *IEEE Trans. Magn.*, 1978, **14**, 975–977.
- A. Rosset, L. Spadola and O. Ratib, Osirix: An Open-Source Software for Navigating in Multidimensional Dicom Images, *J. Digit. Imag.*, 2004, **17**, 205–216.
- A. Angulo-Molina, M. Á. Méndez-Rojas, T. Palacios-Hernández, O. E. Contreras-López, G. A. Hirata-Flores,

- J. C. Flores-Alonso, S. Merino-Contreras, O. Valenzuela, J. Hernández and J. Reyes-Leyva, Magnetite Nanoparticles Functionalized with α -Tocopheryl Succinate (α -TOS) Promote Selective Cervical Cancer Cell Death, *J. Nanopart. Res.*, 2014, **16**, 1–12.
- 25 C. Pereira, A. M. Pereira, C. Fernandes, M. Rocha, R. Mendes, M. P. Fernandez-Garcia, A. Guedes, P. B. Tavares, J.-M. Grenèche, J. P. Araujo and C. Freire, Superparamagnetic MFe_2O_4 ($M = Fe, Co, Mn$) Nanoparticles: Tuning the Particle Size and Magnetic Properties through a Novel One-Step Coprecipitation Route, *Chem. Mater.*, 2012, **24**, 1496–1504.
- 26 P. Tartaj, M. d. P. Morales, S. Veintemillas-Verdaguer, T. González-Carreño and C. J. Serna, The Preparation of Magnetic Nanoparticles for Applications in Biomedicine, *J. Phys. D: Appl. Phys.*, 2003, **36**, R182–R197.
- 27 H.-M. Song, J. I. Zink and N. M. Khashab, Seeded Growth of Ferrite Nanoparticles from Mn Oxides: Observation of Anomalies in Magnetic Transitions, *Phys. Chem. Chem. Phys.*, 2015, **17**, 18825–18833.
- 28 G. Muralidharan, L. Subramanian, S. K. Nallamuthu, V. Santhanam and S. Kumar, Effect of Reagent Addition Rate and Temperature on Synthesis of Gold Nanoparticles in Microemulsion Route, *Ind. Eng. Chem. Res.*, 2011, **50**, 8786–8791.
- 29 R. P. Araújo-Neto, E. L. Silva-Freitas, J. F. Carvalho, T. R. F. Pontes, K. L. Silva, I. H. M. Damasceno, E. S. T. Egito, A. L. Dantas, M. A. Morales and A. S. Carriço, Monodisperse Sodium Oleate Coated Magnetite High Susceptibility Nanoparticles for Hyperthermia Applications, *J. Magn. Magn. Mater.*, 2014, **364**, 72–79.
- 30 B. Issa, S. Qadri, I. M. Obaidat, R. W. Bowtell and Y. Haik, Peg Coating Reduces Nmr Relaxivity of $Mn_{0.5}Zn_{0.5}Gd_{0.02}Fe_{1.98}O_4$ Hyperthermia Nanoparticles, *J. Magn. Reson. Imag.*, 2011, **34**, 1192–1198.
- 31 B. Bittova, J. P. Vejpravova, M. P. Del Morales, A. G. Roca, D. Niznansky and A. Mantlikova, Influence of Aggregate Coating on Relaxations in the Systems of Iron Oxide Nanoparticles, *Nano*, 2012, **07**, 1250004.
- 32 R. H. Kodama, Magnetic Nanoparticles, *J. Magn. Magn. Mater.*, 1999, **200**, 359–372.
- 33 V. Russier, C. de Montferrand, Y. Lalatonne and L. Motte, Size and Polydispersity Effect on the Magnetization of Densely Packed Magnetic Nanoparticles, *J. Appl. Phys.*, 2012, **112**, 073926.
- 34 W. Wei, W. Zhaohui, Y. Taekyung, J. Changzhong and K. Woo-Sik, Recent Progress on Magnetic Iron Oxide Nanoparticles: Synthesis, Surface Functional Strategies and Biomedical Applications, *Sci. Technol. Adv. Mater.*, 2015, **16**, 023501.
- 35 T. E. Torres, E. Lima, A. Mayoral, A. Ibarra, C. Marquina, M. R. Ibarra and G. F. Goya, Validity of the Néel-Arrhenius Model for Highly Anisotropic $Co_xFe_{3-x}O_4$ Nanoparticles, *J. Appl. Phys.*, 2015, **118**, 183902.
- 36 X. Sun, N. Frey Huls, A. Sigdel and S. Sun, Tuning Exchange Bias in Core/Shell FeO/Fe_3O_4 Nanoparticles, *Nano Lett.*, 2012, **12**, 246–251.
- 37 J.-H. Lee, J.-t. Jang, J.-s. Choi, S. H. Moon, S.-h. Noh, J.-w. Kim, J.-G. Kim, I.-S. Kim, K. I. Park and J. Cheon, Exchange-Coupled Magnetic Nanoparticles for Efficient Heat Induction, *Nat. Nanotechnol.*, 2011, **6**, 418–422.
- 38 M. Estrader, A. Lopez-Ortega, S. Estradé, I. V. Golosovsky, G. Salazar-Alvarez, M. Vasilakaki, K. N. Trohidou, M. Varela, D. C. Stanley, M. Sinko, M. J. Pechan, D. J. Keavney, F. Peiró, S. Suriñach, M. D. Baró and J. Nogués, Robust Antiferromagnetic Coupling in Hard-Soft Bi-Magnetic Core/Shell Nanoparticles, *Nat. Commun.*, 2013, **4**, 2960.
- 39 M. Vasilakaki, K. N. Trohidou and J. Nogués, Enhanced Magnetic Properties in Antiferromagnetic-Core/Ferrimagnetic-Shell Nanoparticles, *Sci. Rep.*, 2015, **5**, 9609.
- 40 H. Zeng, J. Li, Z. L. Wang, J. P. Liu and S. H. Sun, Bimagnetic Core/Shell $FePt/Fe_3O_4$ Nanoparticles, *Nano Lett.*, 2004, **4**, 187–190.
- 41 C. Ostefeld and S. Mørup, Magnetic Interactions between Nanoparticles of Different Materials, in *Hyperfine Interactions (C)*, 2002, pp. 83–86.
- 42 S. Mørup, M. F. Hansen and C. Frandsen, Magnetic Interactions between Nanoparticles, *Beilstein J. Nanotechnol.*, 2010, **1**, 182–190.
- 43 P. Gambardella, S. Rusponi, M. Veronese, S. S. Dhesi, C. Grazioli, A. Dallmeyer, I. Cabria, R. Zeller, P. H. Dederichs, K. Kern, C. Carbone and H. Brune, Giant Magnetic Anisotropy of Single Cobalt Atoms and Nanoparticles, *Science*, 2003, **300**, 1130–1133.
- 44 J. Mohapatra, A. Mitra, D. Bahadur and M. Aslam, Surface controlled synthesis of MFe_2O_4 ($M = Mn, Fe, Co, Ni$ and Zn) nanoparticles and their magnetic characteristics, *CrystEngComm*, 2013, **15**, 524–532.
- 45 J. Riegler, J. A. Wells, P. G. Kyrtatos, A. N. Price, Q. A. Pankhurst and M. F. Lythgoe, Targeted Magnetic Delivery and Tracking of Cells Using a Magnetic Resonance Imaging System, *Biomaterials*, 2010, **31**, 5366–5371.
- 46 L. Gutierrez, *et al.*, Synthesis Methods to Prepare Single- and Multi-Core Iron Oxide Nanoparticles for Biomedical Applications, *Dalton Trans.*, 2015, **44**, 2943–2952.
- 47 J. Li, H. Zeng, S. Sun, J. P. Liu and Z. L. Wang, Analyzing the structure of $CoFe-Fe_3O_4$ core-shell nanoparticles by electron imaging and diffraction, *J. Phys. Chem. B*, 2004, **108**, 14005–14008.